Research Square

Preprints are preliminary reports that have not undergone peer review.
They should not be considered conclusive, used to inform clinical practice,
or referenced by the media as validated information.

Research on the Design of Composite Battery Thermal Management System Based on PCM-Finned-Liquid Cooling Plate

Ping Liu
Anhui University of Science and Technology
Zheng Ji
Anhui University of Science and Technology
Zhiwen Wang
Anhui University of Science and Technology
Xiuhe Song
xiuhe.song@ipp.ac.cn

Institute of Energy, Hefei Comprehensive National Science Center
Anhui Yu
State Key Laboratory of Safe Mining of Deep Coal and Environmental Protection
Jing Zhao
State Key Laboratory of Safe Mining of Deep Coal and Environmental Protection

Research Article

Keywords: Lithium ion battery, Battery thermal management system, Phase-change material, Liquid cooling plate

Posted Date: November 20th, 2026

DOI: https://doi.org/10.21203/rs.3.rs-11700043/v1

License: This work is licensed under a Creative Commons Attribution 4.0 International License.
Read Full License

Additional Declarations: No competing interests reported.

Research on the Design of Composite Battery Thermal Management System Based on PCM-Finned-Liquid Cooling Plate

Ping Liu[1], Zheng Ji[1], Zhiwen Wang[1], Xiuhe Song[2*], Anhui Yu[3], Jing Zhao[3]

1.School of Mechatronics Engineering, Anhui University of Science and Technology, Huainan 232001.China

2.Institute of Energy, Hefei Comprehensive National Science Center (Anhui Energy Laboratory)

3.State Key Laboratory of Safe Mining of Deep Coal and Environmental Protection, Huainan Mining (Group) Co., Ltd, Huainan 232000, China

[*]e-mail: xiuhe.song@ipp.ac.cn

Abstract-This study takes the 18650 cylindrical lithium-ion battery pack as the research object. Aiming at the problems of low heat conduction efficiency of the single heat dissipation system of the battery pack and easy failure under high-rate discharge, a composite enhanced heat transfer scheme based on PCM-Fin-Liquid cooling plate is proposed. By comparing and analyzing the temperature control effects of pure phase change cooling, fin-enhanced phase change cooling and composite cooling under 5C high-rate discharge conditions, the technical advantages of the composite cooling scheme are verified. The results show that when the pure phase change material scheme is adopted, the maximum temperature exceeds 326 K. After aluminum fins are implanted in the phase change material, the average temperature of the battery drops to 321.85 K, and the maximum temperature drops to 324.28 K, which are 0.42 K and 0.47 K lower than those of the pure phase change material heat dissipation system, respectively. After the liquid cooling plate is added, the maximum temperature of the battery pack is reduced to below 318 K by the composite cooling system, which is more than 8 K lower than the pure phase change scheme. In addition, considering the influence of the liquid cooling plate structure, cooling liquid flow rate, inlet temperature and ambient temperature on the heat dissipation performance of the composite system, a comprehensive evaluation index θ is constructed by using the weighted normalization method to determine the optimal values of the key parameters in the composite cooling system.

Key word: Lithium ion battery; Battery thermal management system; Phase-change material; Liquid cooling plate.

1. INTRODUCTION

With the intensification of the global energy crisis and the increasingly severe environmental pollution problem, countries around the world have begun to promote the use of clean energy in transportation. Data from the International Energy Agency shows that the transportation sector contributes more than 20% of global carbon dioxide emissions, and the average mole fraction of carbon dioxide worldwide has risen from 338.9 ppm in 1980 to 416.8 ppm in 2023[1, 2]. Electric vehicles, with their zero-emission and high-efficiency characteristics, are considered an effective solution to the petroleum demand and exhaust emission problems of traditional vehicles[3-6]. Lithium-ion battery

power supplies have been gradually applied in various mining equipment due to their advantages such as high energy density, stable discharge characteristics, and long cycle life.

However, the working temperature has a significant impact on the performance of lithium-ion batteries. The optimal working temperature has been determined through research to be between 20℃ and 40℃, and the suitable storage temperature is between 0 ℃and 50℃[7-9]. Pesaran et al.'s research indicates that the temperature range of 15℃ to 35℃ is the optimal performance range for batteries. When the battery temperature is too high, it will accelerate battery aging and reduce the capacity retention rate. Motloch et al.'s experiments show that when the battery temperature is between 40℃ and 50℃, a 1℃ increase in temperature will lead to a decrease in battery life of about two months[10]. In severe cases, excessively high temperatures may cause thermal runaway accidents such as fires[11, 12]. In addition, the temperature uniformity within the battery module is equally crucial. A temperature difference of more than 5℃ will cause inconsistent aging rates among individual cells, thereby affecting the overall service life and safety performance of the battery pack[13, 14].

Currently, common battery thermal management methods include air cooling, phase change material cooling, liquid cooling, heat pipe cooling, and hybrid cooling that combines multiple methods[15-18]. Given the performance limitations of single cooling methods, hybrid thermal management systems that combine multiple cooling methods are receiving increasing attention. Hybrid cooling systems can comprehensively utilize the advantages of different cooling methods and make up for their respective shortcomings, thereby achieving better overall thermal management effects[19, 20]. Murugan et al. conducted a comprehensive review of thermal management methods for electric vehicle battery packs, analyzed the efficiency and impact of different cooling mechanisms such as liquid cooling, air cooling, and phase change materials, and evaluated emerging thermal management technologies[21].

The coupling of phase change materials (PCMs) and liquid cooling is one of the most actively researched hybrid cooling solutions at present. In this composite system, the battery is wrapped with PCMs, and its heat is absorbed by the latent heat of the PCMs, which serves to buffer and homogenize the temperature. The liquid cooling system is responsible for removing the accumulated heat from the PCMs, restoring their heat storage capacity, and thus ensuring the continuous heat dissipation capability of the system. Zhao et al. comprehensively reviewed the coupling of PCMs and liquid cooling, analyzed the key factors influencing the cooling effect of the coupled system and their causes, and discussed the development prospects of thermal management systems based on pure PCMs[22].

Yang et al. designed a lightweight hybrid battery thermal management system that combines heat pipes with composite fins, and achieved excellent thermal management performance by integrating Z-shaped cold plates and PCM composites[23]. Mousavi et al. proposed an improved hybrid thermal management system integrating microchannels and PCMs for the temperature control of square lithium-ion batteries[24]. Jiang et al. studied the cooling board and PCMs and found that under high-temperature and high-discharge conditions, when only PCMs were used for cooling, there was excessive temperature and internal heat accumulation. After adding a coolant at 0.5 m/s, the arrangement distance between batteries could be shortened to 3 mm[25].

Choi et al. conducted a comparative assessment of three liquid-cooled battery thermal management systems: fin cooling, PCM cooling, and inter-cell cooling. Under fast-charging conditions, inter-cell cooling could continuously meet or exceed the target temperature requirements, while fin cooling faced challenges. The study pointed out that effectively controlling the coolant temperature is the key factor for achieving the best PCM cooling effect, and the temperature difference could be reduced by 4.3 K[26]. The latest research has also explored a compact and lightweight hybrid thermal management solution integrating honeycomb structures with PCMs and liquid cooling. By optimizing the hexagonal PCM configuration, the highest comprehensive heat transfer performance was achieved, with PEC values 30.7% and 7.8% higher than other designs[27].

In terms of innovative design of hybrid thermal management systems, El Kassar et al. summarized the latest progress in the integration of lithium-ion batteries and thermal management systems[28]. Luo et al. investigated the enhancement of thermal performance of a battery thermal management system combining snowflake fins and liquid cooling with PCMs under high ambient temperature and high discharge rate conditions[29]. Abd et al. developed a hybrid battery thermal management system integrating aluminum fins and forced air with PCMs[30]. Sutheesh et al. studied the thermal performance of lithium-ion batteries under dry conditions using a hybrid cooling system through numerical and experimental methods[31].

Although hybrid cooling system combines the stability of passive cooling with the efficiency of active cooling, they also have problems such as high system complexity and high cost. How to simplify the system and optimize costs while ensuring performance is an important direction for future research. In addition, issues such as the coordinated control strategies among different cooling methods in the hybrid system and the selection of the optimal operating mode under different conditions also need in-depth study. To address these issues, this paper takes the 18650 cylindrical lithium-ion battery pack as the research object and focuses on the composite battery thermal management system of PCM-fins-liquid cooling plates. It aims to provide design references and theoretical basis for the next generation of efficient, compact, and lightweight battery thermal management systems.

2. MODEL AND CALCULATION METHOD

2.1 Physical Model of the Composite Cooling System

Taking the 18650 cylindrical lithium-ion battery as the research object, the various parameters of the battery are shown in Table 1. The composite cooling system is mainly composed of four core components: phase change material, metal fins, cylindrical lithium-ion battery pack and bottom liquid cooling plate. Its overall architecture is shown in Fig. 1.

Table 1 Battery physical properties

Physical property	Numerical
Capacity	2.5 Ah
Battery diameter	18 mm
Battery height	65 mm
Charging cut-off voltage	3.7 V

End-off voltage	2.75 V
Maximum charging current	5 A
Max Discharge current	12.5 A
Operating temperature	recharge：0~45℃，discharge：-20~60℃

In this composite cooling structure, the phase change material is filled in the gap areas between battery cells, and its main function is to absorb the latent heat during the phase change process to buffer the heat generated during battery discharge. The metal fins are distributed throughout the phase change material, forming an efficient heat conduction channel network, effectively compensating for the inherent defect of the low thermal conductivity of the phase change material. Nine 18650 cylindrical lithium-ion batteries are arranged in a regular array as the main heat source of the entire system. The bottom of the battery pack is equipped with a liquid cooling plate, continuously conducting heat to the external environment.

The overall shape of the composite cooling system is a rectangular prism. Both the length and width are 110 mm, and the total height of the system is 65 mm. There is a uniform spacing of 18 mm between the battery cells to ensure that the phase change material has sufficient filling space. The liquid cooling plate is made of aluminum processing, and the cross-sectional dimensions of the flow channels and the inlet and outlet are both 6 mm × 3 mm.

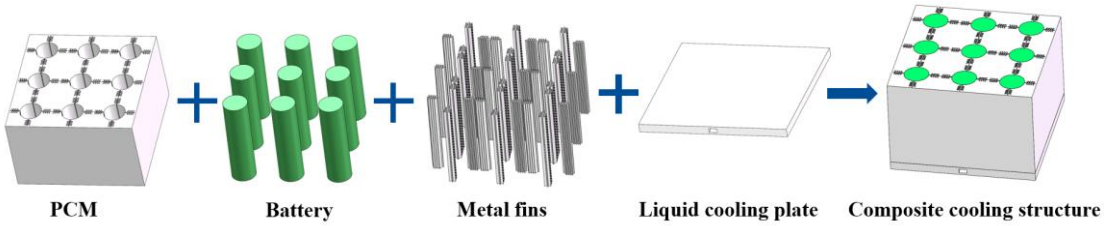

Fig. 1. Structure diagram of the composite cooling system

2.2 Heat generation model of lithium-ion batteries

Accurately calculating the heat generation of batteries is the core link in thermal simulation analysis. In engineering applications, the heat generation model proposed by Bernardi et al. in 1985 has been widely adopted due to its simple form and clear physical meaning[32]. The total heat generation rate can be expressed as:

$$q = \frac{I}{V_b}\left[(E-U)+T\frac{\partial E}{\partial T}\right] = \frac{1}{V}\left[I^2\left(R_j+R_p\right)+IT\frac{\partial E}{\partial T}\right] \quad (1)$$

In the formula, I represents the charging and discharging current of the battery, measured in amperes (A), with positive values indicating discharge and negative values indicating charging; V represents the volume of the battery, measured in cubic meters (m^3); E represents the open-circuit voltage of the battery, which is the battery electromotive force, measured in volts (V); U represents the operating voltage of the battery, also measured in volts (V), and T represents the battery temperature, measured in Kelvin (K). And $I^2(R_j+R_p)$ represent the battery joule heat and polarization heat, respectively. $IT\frac{\partial E}{\partial T}$ represents the reversible reaction heat, which has a relatively small impact on the battery's heat

generation and is usually set as an empirical constant.

During the constant current discharge process, the formula for calculating the battery's SOC is:

$$SOC = 1 - \frac{\eta \int_0^t I\,dt}{Q} \times 100\% \tag{2}$$

In the formula, I represents the discharge current of the battery, A; t represents the discharge time of the battery, h; η represents the discharge efficiency of the battery; Q represents the rated capacity of the battery, Ah.

After fitting the equivalent internal resistance, it was introduced into the calculation process of the heat generation formula, thereby creating a thermal effect model for 18650 lithium-ion batteries. To ensure that the heat transfer process of the battery could be more accurately simulated, UDF was used in the Fluent software to implement dynamic characterization on the heat source. This method can automatically adjust the heat source according to the current state of the battery, thereby improving the accuracy of the simulation results.

2.3 Boundary Conditions and Simulation Working Condition Design

In the numerical simulation, the heat transfer between the outer wall of the system and the surrounding air is treated as natural convection, and the comprehensive heat transfer coefficient is set at 5 $W \cdot m^{-2} \cdot K^{-1}$. The inlet of the liquid cooling plate is defined as a mass flow inlet, with the initial mass flow rate set at 2 g/s. The temperature of the cooling medium at the inlet is the same as the ambient temperature, both maintained at 298.15 K. The liquid cooling plate is set as a pressure outlet, with the reference value of standard atmospheric pressure at 0 Pa as the relative pressure. The initial temperature field of the entire computational domain is uniformly set at 298.15 K.

Considering the complexity of the actual physical process, in order to make the numerical calculation operable and ensure reasonable calculation efficiency, without significantly affecting the accuracy of the results, the following simplification assumptions are made for the simulation model:

（1） Ignore the phase change materials, metal structure and surface plate fin the contact between the interface thermal resistance effect, as an ideal thermal contact state;

（2） The coolant is regarded as a Newtonian incompressible fluid, and its physical parameters remain unchanged.

（3） The influence of local hotspots such as the TAB area of lithium-ion batteries is not taken into account.

（4） The thermophysical properties of aluminum alloy cold plates do not change with temperature and are calculated using fixed parameters.

T The flow state of the coolant inside the liquid cooling plate directly affects the convective heat transfer intensity and the selection of numerical solution strategies. The Reynolds number is used to represent the relative value of viscous force and fluid inertial force, and its mathematical definition formula is:

$$Re = \frac{\rho_f U_{in} D_h}{\mu_f} \tag{3}$$

In the formula, ρ_f as the cooling fluid density, $kg \cdot m^{-3}$; U_{in} as the inlet velocity, m·s; D_h for

hydraulic diameter, m; μ_f represents the dynamic viscosity of the coolant, Pa·s.

The definition formula of the hydraulic diameter D_h for non-circular cross-section flow channels is:

$$D_h = \frac{4A_c}{p} = \frac{2wh}{w+h} \tag{4}$$

In the formula: A_C is the cross-sectional area of the flow channel, m²; p represents the wet perimeter length, m; w and h are respectively the width and height of the rectangular flow channel, m.

Based on the basic theory of fluid mechanics, the geometric dimensions and flow parameters of the flow channels involved in this study were substituted into the above formula for calculation. The results show that the Reynolds number of the coolant is much less than the critical value of 2300 for the upper limit of laminar flow. Therefore, it can be confirmed that the coolant flow inside the liquid cooling plate is in a laminar state.

The flow and heat transfer process of the coolant in the flow channel of the liquid cooling plate follow the three fundamental laws of conservation of mass, momentum and energy. For Newtonian incompressible fluids, the above conservation laws can be expressed in the form of the following partial differential equations.

Momentum equation：

$$\begin{aligned}
\frac{\partial \rho u}{\partial t} + \nabla(\rho u U) &= -\frac{\partial P}{\partial x} + \frac{\partial \tau_{xx}}{\partial x} + \frac{\partial \tau_{yx}}{\partial y} + \frac{\partial \tau_{zx}}{\partial z} + F_x \\
\frac{\partial \rho v}{\partial t} + \nabla(\rho v U) &= -\frac{\partial P}{\partial y} + \frac{\partial \tau_{xy}}{\partial x} + \frac{\partial \tau_{yy}}{\partial y} + \frac{\partial \tau_{zy}}{\partial z} + F_y \\
\frac{\partial \rho w}{\partial t} + \nabla(\rho w U) &= -\frac{\partial P}{\partial z} + \frac{\partial \tau_{xz}}{\partial x} + \frac{\partial \tau_{yz}}{\partial y} + \frac{\partial \tau_{zz}}{\partial z} + F_z
\end{aligned} \tag{5}$$

energy equation：

$$(\rho U T) = \frac{\partial}{\partial x}\left(\frac{k}{C_p}\frac{\partial T}{\partial x}\right) + \frac{\partial}{\partial y}\left(\frac{k}{C_p}\frac{\partial T}{\partial y}\right) + \frac{\partial}{\partial z}\left(\frac{k}{C_p}\frac{\partial T}{\partial z}\right) + S_T \tag{6}$$

equation of continuity：

$$\frac{\partial \rho}{\partial t} + \frac{\partial(\rho u)}{\partial x} + \frac{\partial(\rho v)}{\partial y} + \frac{\partial(\rho w)}{\partial z} = 0 \tag{7}$$

The meanings of each symbol in the above system of equations are as follows: represents the fluid density; *u, v, w* are the components of the velocity vector in the *x, y,* and *z* coordinate directions respectively; *P* is the static pressure exerted on the fluid element; is the component of the viscous stress tensor; *F* is the volume force; *T* is the temperature; C_p is the specific heat capacity at constant pressure; *k* is the thermal conductivity coefficient; S_T is the viscous dissipation term and internal heat source term.

2.4 Grid Division and Independence Verification

To eliminate the interference of grid density on the numerical calculation results, a grid independence verification analysis needs to be conducted. As shown in Fig. 2, in this verification, six different-sized grid schemes were selected, with the number of elements being 938325, 1653276, 2157253, 2756325, and 3346726 respectively. Under the same simulation conditions, transient heat flow

coupling calculations were carried out, and the trend of the maximum temperature on the battery surface with respect to the grid density was monitored. The calculation results show that when the total number of grids exceeds 2756325, the obtained maximum temperature value tends to stabilize, and the temperature deviation between adjacent schemes remains within 0.05 K. After comprehensively considering the two factors of calculation accuracy and time cost, the subsequent numerical simulation uniformly adopts a grid configuration of 2756325 elements.

2.5 Experimental Verification

In this study, a commercial 18650 cylindrical lithium-ion battery was selected as the test object, with a nominal capacity of 2.5 Ah and a rated voltage of 3.7 V. The experiment used the Xin Rui CT-4008-5V20A battery charging and discharging tester, and a multi-channel data acquisition instrument was used to record the temperature changes at each measurement point on the battery surface. The environmental temperature was 298.15 K, and the discharge rate was 1-5C. The schematic diagram of the entire experimental device is shown in Fig. 3(a). To verify the accuracy of the established thermal simulation model, experiments were conducted at discharge rates of 3C, 4C, and 5C, and the measured battery surface temperatures were compared with the simulation calculation results. The temperature deviation is shown in Fig. 3(b).

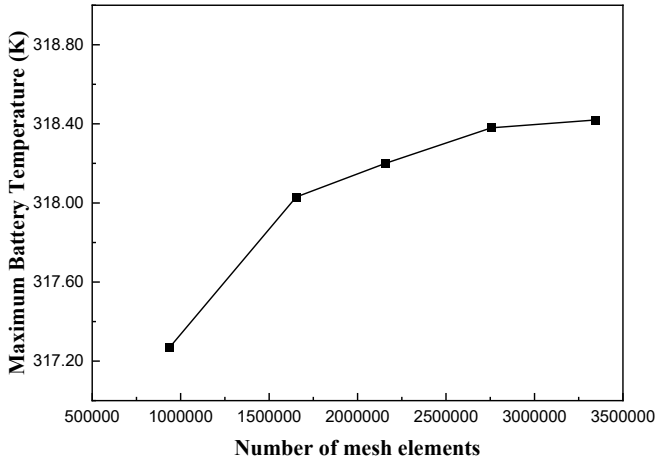

Fig. 2. Verification of grid independence

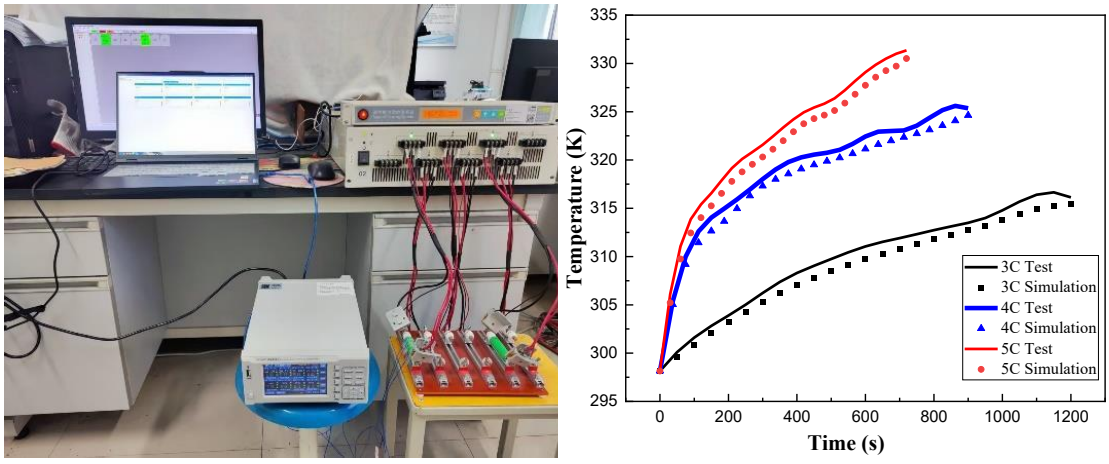

Fig. 3. (a)Experimental system diagram and (b) Comparison of experimental and simulated surface temperatures of batteries at 3-5Cdischarge rates

As shown in the figure, the deviations between the simulated temperature and the experimental temperature in all three charging conditions remained at a relatively low level. Specifically, in the 3C charging condition, the temperature deviation fluctuated between 0.54 and 1.51 K; in the 4C charging condition, the temperature deviation was 0.37 to 1.59 K; and in the 5C charging condition, the temperature deviation was relatively stable, ranging from 0.85 to 1.43 K. Overall, the temperature deviations in all conditions did not exceed 1.6 K, and the maximum relative error was less than 0.5%, indicating that the battery heat generation model and heat transfer model established in this paper can accurately predict the temperature rise behavior of 18650 lithium-ion batteries under different discharge rates, and can provide reliable simulation basis for the subsequent optimization design of the thermal management system.

3. RESULTS AND DISCUSSION

3.1 Thermal Management Performance Analysis of Battery Packs under Different Cooling Method Combinations

3.1.1 Three cooling methods

To systematically evaluate the performance advantages of the composite cooling scheme, this study designed three sets of schemes, respectively examining the performance differences of a single phase change material cooling, the collaborative cooling of the phase change material and metal fins, and the composite cooling with the addition of a liquid cooling plate under the same operating conditions.

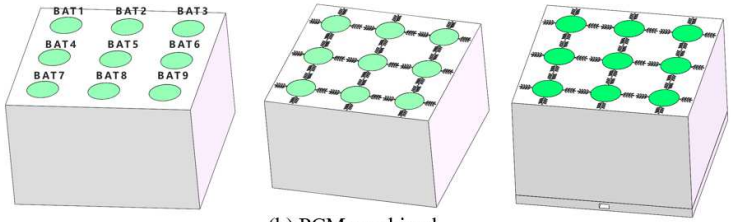

Fig. 4. Structural Diagram of Three Cooling Methods

Fig. 4 shows the cooling methods of the three schemes. Scheme one only fills the battery compartments with the phase change material, relying on the latent heat of phase change and thermal conductivity of the material to achieve passive heat dissipation; scheme two embeds metal fins on the basis of the phase change material, constructing a rapid heat transfer path throughout the phase change material area through the high thermal conductivity of the fins; scheme three adds a liquid cooling plate on top of the former two to form an active heat extraction channel. The batteries are sequentially numbered in the figure to facilitate the subsequent study of the temperatures of each individual battery.

3.1.2 The temperature distribution pattern of each individual battery cell

Fig. 5 presents a quantitative comparison of the surface temperatures of nine batteries. In the pure phase change material scheme, the temperatures of the batteries exhibit a distinct pattern of high in the middle and low at the edges: BAT5, located at the center of the array, has the highest temperature at 326.2 K, while the four corner batteries, BAT1, BAT3, BAT7, and BAT9, have relatively lower temperatures,

ranging from 325.5 to 325.8 K. This reflects the influence of geometric position on the heat dissipation path. The central battery is surrounded by adjacent cells, and heat can only diffuse outward through a limited number of phase change material layers; the corner batteries, on the other hand, have two or three heat dissipation surfaces, facilitating more convenient heat exchange with the external environment. The maximum temperature difference reaches 0.7 K, which may seem small in value, but considering that the overall temperature level is already close to the safety limit, this difference is sufficient to cause consistency issues in the battery pack.

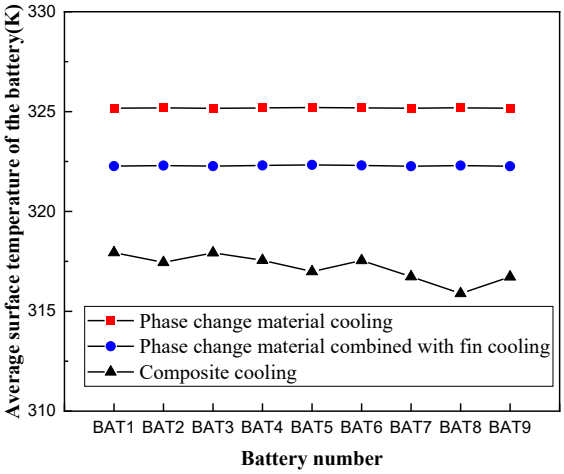

Fig. 5. Battery temperature comparison chart for three cooling methods

After adding fins, the temperature distribution curve shifts downward by approximately 3 K. The temperature of BAT5 drops to 323.4 K, and the edge batteries' temperatures fall to 322.7 - 323.0 K, with the maximum temperature difference slightly narrowing to 0.7 K. Notably, although the fin scheme reduces the absolute temperature, the improvement in uniformity is limited. This is because while the fins enhance the thermal conductivity, they do not fundamentally change the boundary conditions for heat dissipation. The system still relies on natural convection with the external environment, and the heat transfer coefficients of these two mechanisms are low and unevenly distributed in space. The ends of the fins located inside the system have difficulty obtaining sufficient heat exchange area, reducing the enhancement effect in the central region.

The temperature curve of the hybrid cooling scheme shows two significant features: first, the overall temperature level drops further by approximately 5 K, with the temperature range of the nine batteries concentrated between 316.8 and 318.2 K; second, and more importantly, the temperature distribution curve tends to flatten, with the maximum temperature difference compressed to 1.4 K. The key to this improvement lies in the liquid cooling plate providing uniform and stable bottom boundary cooling. Regardless of the battery's position in the array, its bottom surface is separated from the cooling fluid with a constant inlet temperature by only a thin aluminum plate, resulting in a consistent thermal resistance.

3.1.3 Comparison of temperature distribution characteristics of battery packs with different cooling methods

After continuous discharge at a 5C rate for 720 seconds, the temperature field distribution of the three cooling schemes showed significant differences. As can be observed from the overall temperature

cloud map shown in Fig. 6, when using the pure phase change material scheme, a large number of high-temperature areas were present on the battery surface, especially for the BAT5 battery located at the center of the array, with the highest temperature exceeding 326 K. The fundamental reason for this phenomenon lies in the fact that although the paraffin-based phase change material has a relatively high latent heat of phase change, its thermal conductivity is much lower than that of metal materials. When the battery is discharged at a 5C high rate, the heat generation power is large, and the high heat flux density is transferred outward through the low thermal conductivity medium, resulting in a significant thermal accumulation near the battery surface.

After implanting aluminum fins in the phase change material, the distribution characteristics of the temperature field have undergone significant changes. The surface temperature of the battery has dropped, and the maximum temperature has decreased. This improvement is due to the introduction of the fins, which establish multiple high-conductivity channels in the system, quickly guiding the heat on the battery surface to the far end of the phase change material area, significantly shortening the transmission distance of heat from the heat source to the heat dissipation surface.

The complete composite cooling scheme demonstrated the most superior temperature control effect, with the highest temperature controlled below 318 K, a reduction of more than 8 K compared to the pure phase change scheme. This significant progress is attributed to the forced convective cooling mechanism of the liquid cooling plate. The circulating cooling fluid in the bottom liquid cooling plate passes through each battery unit below, and the uniformity of the temperature field was significantly improved.

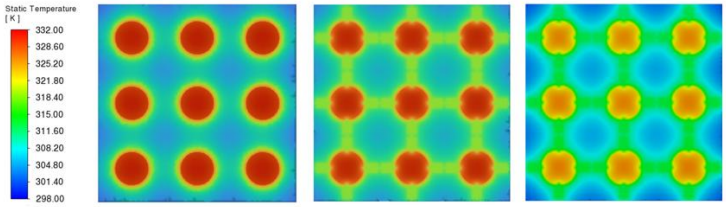

(a) PCM cooling (b) PCM combined with finned cooling (c) Composite cooling

Fig. 6. Overall temperature cloud of the three cooling methods

3.2 Key Parameter Analysis of the Liquid Cooling Plate in the Composite Cooling System

As the core component accountable for active heat dissipation within the system, the geometric arrangement of internal flow channels in liquid-cooled plates exerts a decisive influence on the overall performance. This study meets the battery cooling requirements through the design and comparison of three typical channel configurations: parallel liquid cooling channels, intermittent liquid cooling channels, and oblique cut liquid cooling channels, as depicted in Fig. 7. To identify the optimal channel configuration, comparative analyses were carried out on the three types of liquid-cooled plates. Moreover, to ascertain the most favorable operating conditions for the cooling system, the impacts of coolant flow rate, inlet temperature, and ambient temperature on heat dissipation performance were examined. Subsequently, the optimal combined cooling solution was determined by means of comprehensive performance evaluation criteria.

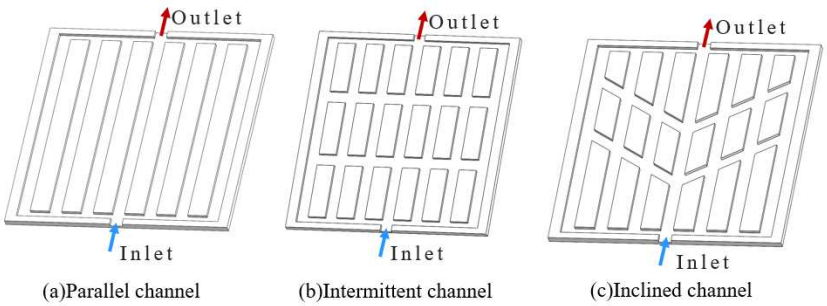

(a)Parallel channel (b)Intermittent channel (c)Inclined channel

Fig. 7. Three different liquid cooling plate structures

3.2.1 Analysis of Heat Dissipation Performance of Different Liquid Cooling Plate Structures

From the temperature distribution of the battery surface shown in Fig. 8, it can be seen that the three liquid cooling plate structures have systematic differences in the cooling effect on the nine battery cells. Under the parallel liquid cooling channel scheme, the temperatures of each battery show a relatively obvious gradient distribution: BAT1, BAT2, and BAT3 are located in the entrance area, with relatively lower temperatures, maintained at 318.80 - 319 K; as the cooling fluid moves along the flow path towards the outlet, its own temperature gradually increases due to continuous heat absorption, and the convective heat transfer capacity decreases accordingly, resulting in a reduction in the cooling effect of the outlet-side batteries such as BAT7, BAT8, and BAT9, with their temperatures rising to 319.20 - 319.40 K. This temperature distribution of cold at the entrance and hot at the exit is because the fluid in the parallel liquid cooling channels flows stably in a laminar state. Once the boundary layer is established, it gradually thickens along the path, and the velocity near the wall decreases, resulting in a downward trend in the convective heat transfer coefficient. There is no lateral fluid exchange between each branch, and no cross-channel mass and energy transfer can be used to balance the temperature differences.

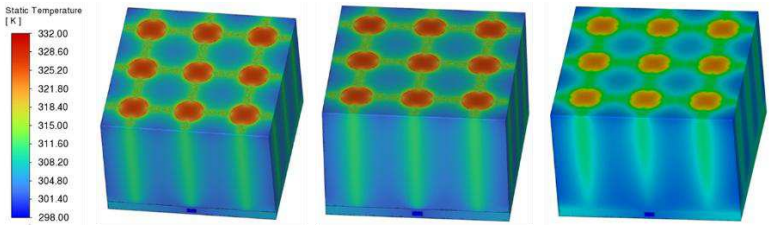

Fig. 8. Cloud chart of working temperatures for three types of liquid-cooled plate batteries

As can be observed from Fig. 9, the overall temperature level of the intermittent liquid cooling channels is lower compared to the parallel liquid cooling channels. The average temperature of the nine batteries is approximately 317.3 K, which is about 0.4 K lower than that of the parallel liquid cooling channels. The temperatures of each battery fluctuate. This non-monotonic distribution is due to the periodic disturbance of the convective field caused by the intermittent separators. When the cooling fluid reaches the end of the branch, it is forced to make a sharp turn into the adjacent channel. This process involves a sudden change in flow direction, intense curvature of streamlines, and local acceleration of flow velocity. The secondary flow and vortex structures generated in the turning area disrupt the original boundary layer, allowing the fluid near the wall to be updated, and significantly enhancing local convective heat transfer.

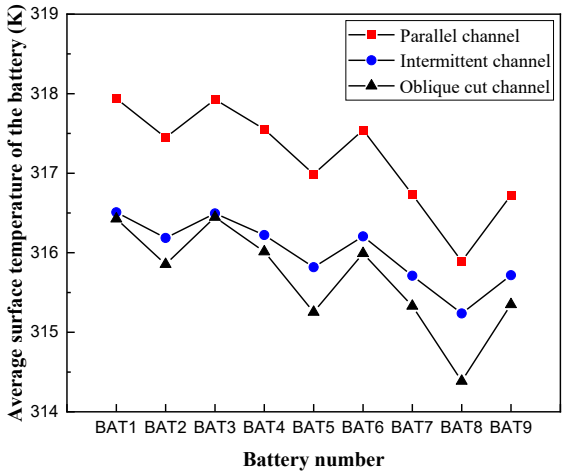

Fig. 9. Average surface temperatures of each battery under three liquid-cooling configurations

The temperatures of the nine batteries in the Oblique cut channel liquid cooling are highly concentrated between 316.8 - 317.3 K. In the Oblique cut channel liquid cooling, the cooling liquid no longer flows in a single direction but flows among multiple inclined channels arranged in an inclined manner. This structure enables the high-temperature fluid and the low-temperature fluid to be fully mixed, and the heat transfer conditions in each area tend to be consistent. From the temperature data, the highest temperature of the batteries in the Oblique cut channel liquid cooling is 317.4 K, about 1.5 K lower than that of the parallel liquid cooling channel and about 1.1 K lower than that of the intermittent liquid cooling channel.

From the Fig. 10 can be seen that the three-dimensional temperature cloud map of the battery pack. The batteries located at the edge of the array have a lower temperature compared to those in the middle. This is because the batteries at the edge have more lateral heat dissipation surfaces, which can directly conduct natural convection with the external environment. The heat dissipation performance of different liquid cooling channels is different. The temperature distribution of the Oblique cut channel liquid cooling channel is more uniform, which improves the uniformity of the battery pack. Each battery bottom no longer corresponds to a single flow path, but is simultaneously cooled by multiple Oblique cut channel liquid cooling channels in an alternating manner. The coolant continuously converges, splits, and mixes at each node of the channel grid. The heat in the high-temperature area is quickly diffused throughout the system, while the low-temperature area receives heat replenishment. Eventually, the entire battery pack reaches a state of thermal balance.

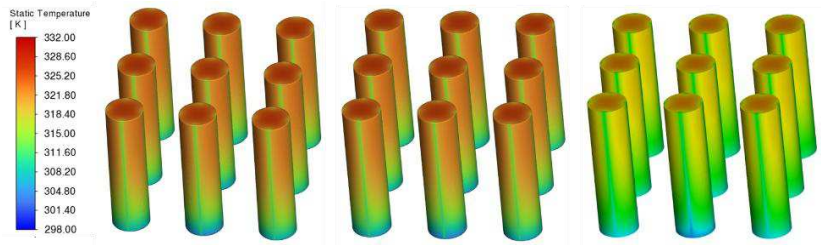

Fig. 10. Temperature cloud maps of battery packs in three composite cooling systems

Fig. 11 visually presents the comparison of key performance indicators among the three liquid cooling plate structures. From the perspective of the maximum surface temperature T_{max} of the battery, the parallel liquid cooling channel is 318.92 K, the intermittent liquid cooling channel drops to 317.46

K, and the inclined broken liquid cooling channel further decreases to 317.42 K. The intermittent liquid cooling channel achieved a cooling rate of 1.46K compared with the parallel liquid cooling channel. The reduction rate of the inclined liquid cooling channel compared with the parallel liquid cooling channel reaches 1.5K.

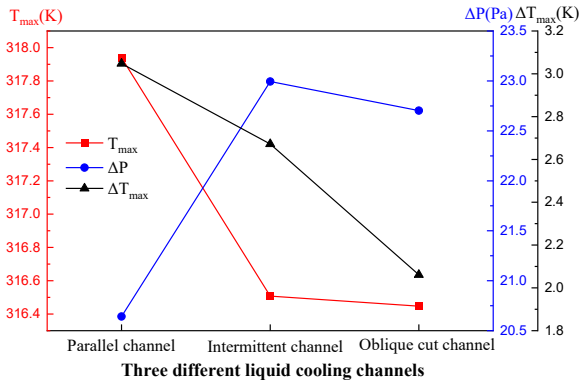

Fig. 11. Impact of three liquid-cooling configurations on system thermal performance

Battery maximum temperature difference ΔT_{max} contrast reveals the structure of three kinds of control ability difference of temperature field uniformity. The maximum temperature difference of the parallel liquid cooling channel is 3.05K, that of the intermittent liquid cooling channel is 2.06K, and the oblique liquid cooling channel reduces the maximum temperature difference to 2.67K. This is attributed to the more periodic destruction of the boundary layer and the local redistribution of heat flow in the intermittent and oblique regions.

The comparison of the pressure drop ΔP of the liquid cooling system reflects the flow resistance characteristics and energy consumption levels of the three structures. The pressure drop of the parallel liquid cooling channel is 20.64 Pa, which is the lowest among the three. The pressure drop of the intermittent liquid cooling channel system increases to 22.99 Pa, an increase of 2.35 Pa compared to the parallel liquid cooling channel. Although the slanted intermittent liquid cooling channel has a complex flow path, due to the use of an inclined rather than a right-angle turn, the change in the fluid direction is relatively gentle, and the local resistance coefficient is smaller; and the grid-like channel provides multiple parallel paths, reducing the pressure drop to 22.70 Pa. From the perspective of energy economy, the parallel liquid cooling channel is the best, the slanted intermittent liquid cooling channel is second, and the intermittent liquid cooling channel is the worst.

Fig. 12 presents the pressure drop cloud diagram inside the liquid cooling plate. In the parallel liquid cooling channel scheme, the inlet area shows a high-pressure zone, and the pressure gradually decreases as it moves upward along each branch until a low-pressure zone is formed at the outlet area. This uniform attenuation of pressure field reflects the characteristic of frictional resistance along the path in the laminar flow state. The pressure drop of each parallel liquid cooling channel is almost exactly the same, and no obvious uneven flow distribution is observed.

The pressure cloud diagram of the intermittent liquid cooling channel shows obvious local high-pressure points. The pressure at the intermittent point near the inlet is relatively high, while the pressure at the intermittent point near the outlet is slightly lower. This may be related to the continuous loss of energy and gradual attenuation of flow velocity after the fluid undergoes multiple turns.

The pressure variation of the Oblique cut channel liquid cooling channel is similar to that of the intermittent liquid cooling channel. The pressure distribution at the connection node of the ribs radiates outward and decreases gradually in all directions.

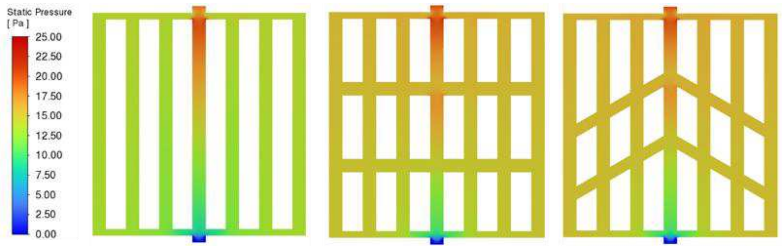

Fig. 12. Pressure drop contour map of three liquid-cooled plate structures

The parallel liquid cooling channels sacrifice basic cooling capacity for low pressure drop, but the cooling effect is limited by the flow direction; the intermittent liquid cooling channels enhance heat exchange at the cost of local pressure, but the energy consumption increases significantly; the Oblique cut channel liquid cooling channels achieve more balanced temperature control performance by means of ingenious biomimetic design, while moderately increasing the pressure drop.

3.2.2 The influence of coolant flow rate on heat dissipation performance

Fig. 13 shows the distribution pattern of the surface temperatures of each battery cell under different mass flow conditions. From the overall trend, as the flow rate gradually increases from 0.5 g/s to 2.5 g/s, the surface temperatures of each battery show a significant downward trend. At the low flow rate of 0.5 g/s, the surface temperatures of BAT1 to BAT3, which are located upstream, are the highest, reaching approximately 319.5 K, 319.2 K, and 319.6 K respectively, while the temperatures of the downstream BAT7 to BAT9 are relatively lower, maintaining below 318.2 K. This temperature distribution inhomogeneity is mainly due to the continuous heat absorption process of the coolant in the flow channels. As the coolant flows along the flow channels, its temperature gradually increases, resulting in a weakened heat transfer driving force for the subsequent batteries.

When the flow rate is increased to 1 g/s, the temperatures of all batteries decrease, but this temperature gradient along the flow channels still exists. Continuing to increase the flow rate to 1.5 g/s and 2 g/s, the temperature distribution gradually becomes more stable, especially at the 2 g/s condition, the temperature difference between BAT1 and BAT9 has narrowed to approximately 1.8 K. However, it is worth noting that when the flow rate is further increased to 2.5 g/s, the improvement effect of the temperature distribution tends to saturate. Although the temperatures of all batteries decrease slightly, the reduction is not as significant as in the previous conditions. This indicates that under the given flow channel structure and heat load conditions, simply relying on increasing the flow rate to improve the heat dissipation effect has a diminishing marginal rule. An excessively high flow rate does not bring significant temperature control benefits.

In addition, regardless of the change in flow rate, BAT8 always shows a relatively lower temperature level because this position is at the coolant inlet, with better heat dissipation effect. From the overall temperature distribution of the battery pack, as the flow rate increases, the uniformity of the temperature field improves, but this improvement is not a linear relationship, but rather shows a fast-then-slow characteristic.

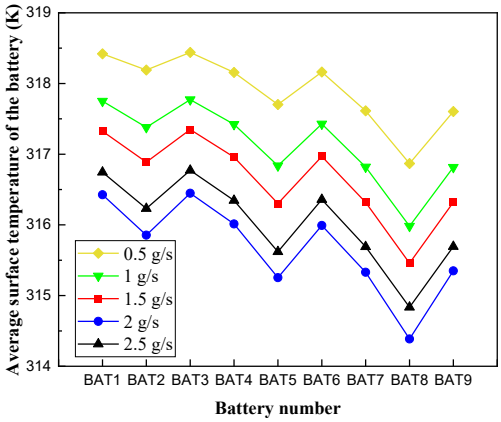

Fig. 13. Average surface temperatures of each cell at different mass flow rates

Under different mass flow rates, Fig. 14 comprehensively presents the changing patterns of three key indicators: the maximum temperature T_{max}, the maximum temperature difference ΔT_{max}, and the system pressure drop ΔP. From the maximum temperature curve, it can be seen that T_{max} decreases monotonically with the increase in flow rate. At the lowest flow rate of 0.5 g/s, $T_{\max}$ reaches 319.5 K, exceeding the recommended working limit of the battery. When the flow rate increases to 1 g/s, T_{max} drops rapidly to 318.8 K, a decrease of approximately 0.7 K. Continuing to increase to 1.5 g/s and 2 g/s, T_{max} drops to 318.4 K and 317.7 K respectively. Analyzing from the perspective of cooling efficiency, the cooling effect between 0.5 g/s and 1 g/s is the most significant, while the improvement between 2 g/s and 2.5 g/s is no longer obvious, with a decrease of only about 0.3 K. This further confirms the law of diminishing marginal benefits brought by increasing the flow rate.

The changing trend of the maximum temperature difference ΔT_{max} is more complex. In the low flow rate range of 0.5 to 1.5 g/s, ΔT_{max} remains basically between 1.6 and 1.8 K. Increasing the flow rate does not significantly improve the temperature uniformity, but when the flow rate enters the range of 1.5 g/s and above, ΔT_{max} shows a fluctuation of first increasing and then decreasing: at 2 g/s, it reaches a peak of approximately 2.0 K, and then drops to approximately 1.9 K at 2.5 g/s. The physical mechanism behind this phenomenon is that although increasing the flow rate enhances the overall heat exchange intensity, it also changes the flow field distribution in the flow channels, possibly generating local vortices or flow dead zones in certain positions, resulting in a decrease in the heat exchange efficiency of some batteries. Therefore, while pursuing high flow rate cooling, attention must be paid to the impact of flow field uniformity on the temperature distribution.

The growth trend of the system pressure drop ΔP is the most obvious. At 0.5 g/s, the pressure drop is only about 4.50 Pa; when the flow rate is doubled to 1 g/s, the pressure drop rises to approximately 9.80 Pa; continuing to increase to 2 g/s, the pressure drop has reached 23.70 Pa; and at the highest flow rate of 2.5 g/s, the pressure drop suddenly increases to 31.2 Pa. This rapid increase in pressure drop conforms to the proportional relationship between pressure drop and the square of flow velocity in fluid mechanics, but an excessively high system pressure drop means that more pump power is required to maintain the flow rate, thereby increasing the energy consumption of the entire thermal management system.

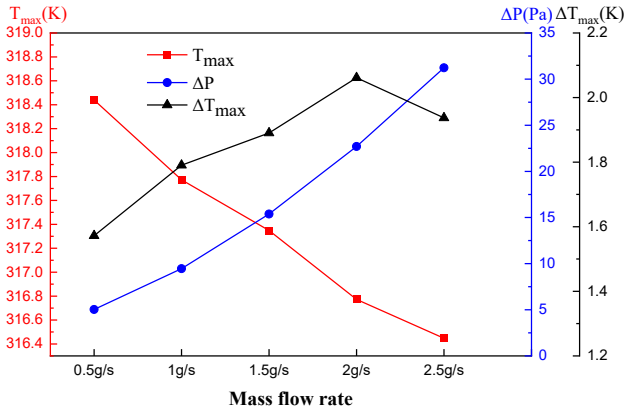

Fig. 14. Thermal performance of battery packs at different mass flow rates

3.2.3 The influence of inlet temperature on heat dissipation performance

Fig. 15 shows the temperature distribution of each cell in the battery pack under different inlet temperatures under the operating condition of a mass flow rate of 2 g/s and a discharge rate of 5C. It can be seen that in the temperature of each battery cell along the flow direction shows a similar fluctuating trend. This indicates that under a constant flow rate, the inlet temperature mainly affects the overall temperature level of the battery, while its influence on the spatial distribution pattern of the temperature field is relatively limited.

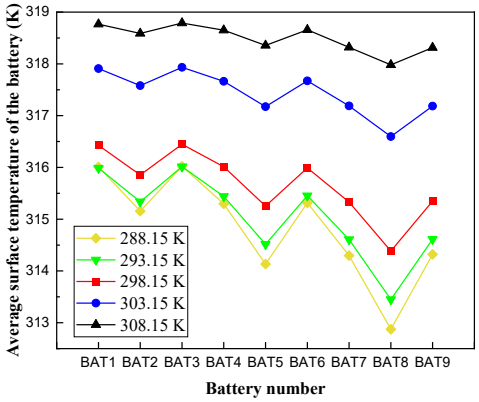

Fig. 15. Temperature distribution of the battery pack at different inlet temperatures

After increasing the inlet temperature of the coolant, the temperature of the individual battery cells showed a synchronous upward trend overall. Specifically, when the inlet temperature was 288.15 K and 293.15 K, the temperature of the battery cells was relatively low, but the temperature difference between different cells was relatively large. However, when the inlet temperature rose to 303.15 K and above, the temperatures of each cell significantly increased, indicating that the heat absorption capacity of the coolant weakened, and local heat was more likely to accumulate in the battery.

For different inlet temperatures of the coolant, Fig. 16 compares the changes in the maximum temperature T_{max} of the battery pack, the maximum temperature difference ΔT_{max}, and the system pressure drop Δp. It can be seen that as the inlet temperature increases, the maximum temperature T_{max} of the battery pack shows a significant upward trend. This is because under the condition of a constant mass flow rate, an increase in the inlet temperature will reduce the temperature difference between the coolant and the battery, thereby weakening the convective heat transfer intensity and making it difficult for the heat generated inside the battery to be removed in a timely manner.

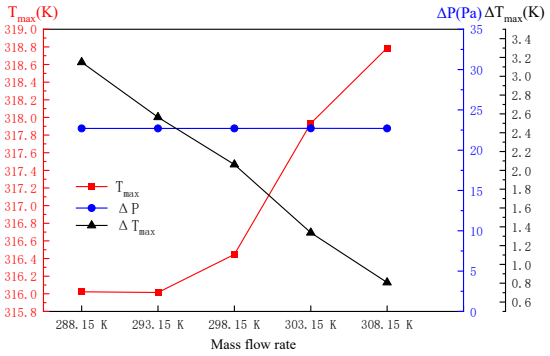

Fig. 16. Thermal performance of battery packs at different inlet temperatures

Contrary to the trend of the maximum temperature change, ΔT_{max} decreases gradually as the inlet temperature rises. This indicates that at higher inlet temperatures, although the overall temperature level of the battery increases, the temperature differences between individual cells are reduced, and the temperature distribution becomes more uniform. This phenomenon is mainly due to the overall weakening of the heat exchange driving force between the battery and the coolant under higher inlet temperature conditions, resulting in a more gradual change in the temperature gradient along the path.

In contrast, the system pressure drop Δp varies little under different inlet temperature conditions and remains within a relatively stable range. This suggests that in this operating condition, the inlet temperature has a limited impact on the flow resistance of the coolant, and the system flow performance is mainly controlled by flow rate and the flow channel structure.

3.2.4 The influence of ambient temperature on heat dissipation performance

Fig. 17 presents the mass flow rate of the coolant at a fixed discharge rate of 5C and a flow rate of 2 g/s, the coolant inlet temperature at 298.15 K, and the surface temperature data of each cell of the battery under different ambient temperatures. In all operating conditions, the temperatures of each cell along the battery arrangement direction show a relatively consistent fluctuation pattern. The high-temperature areas mainly concentrate in the middle and near the outlet side, indicating that the heat exchange conditions in this area are relatively weak. As the ambient temperature increases, the temperature curves of all cells shift upward overall, and the relative distribution patterns of different cells remain basically unchanged. This indicates that under the condition of a fixed coolant inlet temperature, the change in ambient temperature mainly affects the convective heat transfer intensity on the battery surface, thereby raising the overall working temperature of the battery, while having a relatively small impact on the spatial distribution characteristics of the temperature field.

Taking the maximum temperature change trend as an example, when the ambient temperature increases from 293.15 K to 313.15 K, the temperatures of all cells show a significant increase, indicating that the increase in ambient temperature will weaken the cooling capacity of the system and is not conducive to the battery operating within the safe temperature range.

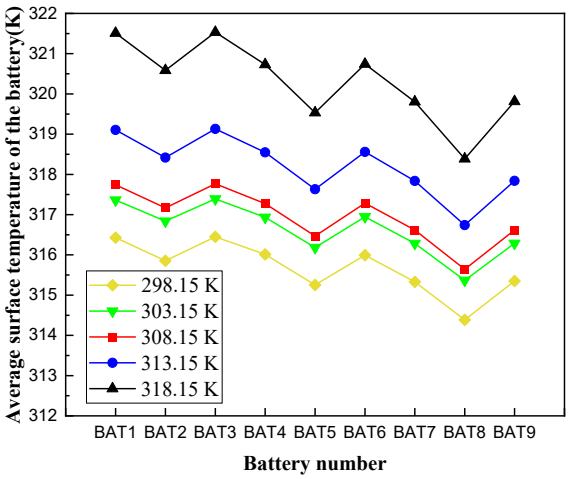

Fig. 17. Temperature distribution of battery packs at different ambient temperatures

Fig. 18 compares the trend of the maximum temperature T_{max}, the maximum temperature difference ΔT_{max}, and the pressure drop Δp of the liquid cooling system under different environmental temperatures. It can be seen that as the environmental temperature increases, T_{max} shows a nearly monotonically increasing trend. This is because when the inlet temperature of the coolant remains constant, an increase in the environmental temperature reduces the heat transfer temperature difference between the outer surface of the battery and the surrounding air, making it more difficult for some heat to escape through the shell to the outside, thereby leading to an exacerbation of heat accumulation inside the battery.

At the same time, ΔT_{max} also gradually increases with the increase in environmental temperature, indicating that the temperature non-uniformity worsens under high environmental temperature conditions. This phenomenon indicates that in high-temperature environments, local weak heat transfer areas are more likely to form hotspots, thereby amplifying the temperature difference level within the battery pack, which is not conducive to maintaining battery lifespan and consistency.

In contrast, the pressure drop Δp of the liquid cooling system varies little with the environmental temperature and remains within a relatively stable range. This is because in this section of the test conditions, the physical parameters of the coolant and the flow rate remain unchanged, and the environmental temperature mainly affects the heat transfer process between the battery and the surrounding air. The influence of the flow resistance inside the flow channel is relatively weak. Therefore, the influence of the environmental temperature on the system's flow performance can be ignored.

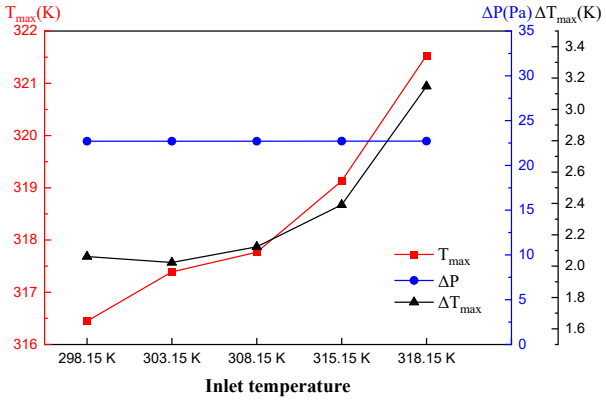

Fig. 18. Heat dissipation performance of the battery pack under different environmental temperatures

3.2.5 Comprehensive Performance Evaluation and Optimal Solution Determination

To overcome the limitations of single-indicator optimization, a comprehensive performance evaluation indicator needs to be introduced. The three independent indicators should be weighted and integrated into a scalar function, so that the multi-objective optimization problem can be transformed into a single-objective problem, making the optimal solution easier to obtain. In this study, the weighted normalization method is used to construct the comprehensive evaluation indicator θ, and its expression is defined as follows[33]:

$$\theta = \mu_1 \frac{X_i - X_{min}}{X_{max} - X_{min}} + \mu_2 \frac{Y_i - Y_{min}}{Y_{max} - Y_{min}} + \mu_3 \frac{Z_i - Z_{min}}{Z_{max} - Z_{min}} \tag{8}$$

In the formula, θ represents the comprehensive performance evaluation index, and the smaller its value indicates better overall system performance; X_i is the highest temperature of the battery surface in the current scheme, X_{min} is the lowest temperature among all candidate schemes, and X_{max} is the highest temperature among all candidate schemes; Y_i is the maximum temperature difference of the battery pack in the current scheme, Y_{min} is the minimum temperature difference among all candidate schemes, and Y_{max} is the maximum temperature difference among all candidate schemes; Z_i is the pressure drop of the liquid cooling system in the current scheme, Z_{min} is the minimum pressure drop among all candidate schemes, and Z_{max} is the maximum pressure drop among all candidate schemes; 1, 2, and 3 are the weight coefficients corresponding to the three indicators, all ranging from 0 to 1, and the sum of the three data is 1.

Using the parameter scanning method for analysis, fix μ_2=μ_3, assign equal weights to temperature difference and pressure drop, let μ_1 vary from 0.20 to 0.50 in steps of 0.05, and adjust μ_2 and μ_3 accordingly to satisfy the constraint μ_1 μ_2 μ_3 = 1. A total of 7 sets of weight combinations are generated, calculate the θ values of the three schemes respectively, and plot the θ-μ_1 relationship curve as shown in.

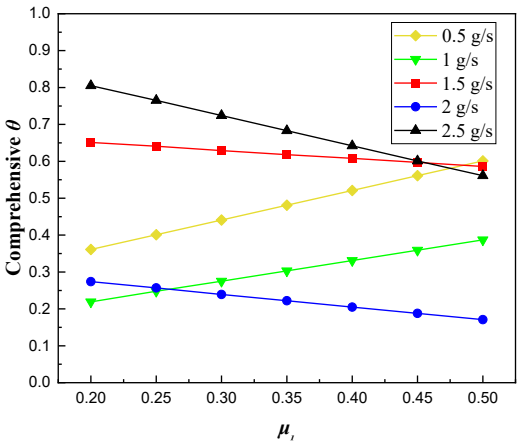

(a) Curve graph showing the relationship between θ - μ_1 and different inlet flow rates

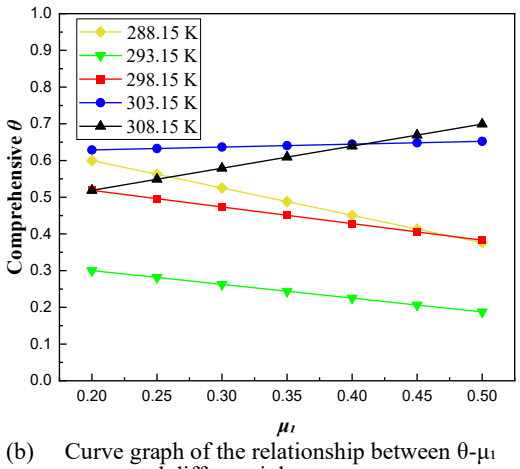

(b) Curve graph of the relationship between θ-μ1 and different inlet temperatures

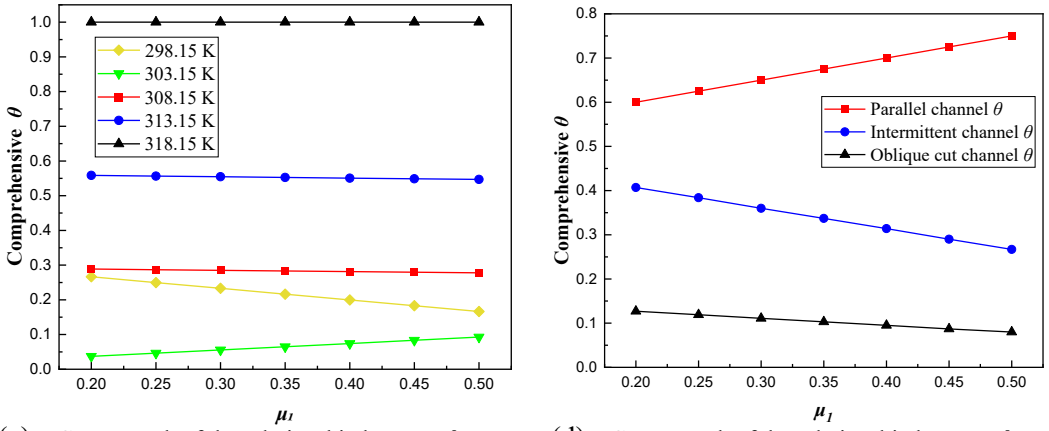

(c) Curve graph of the relationship between θ-μ_1 and different ambient temperatures

(d) Curve graph of the relationship between θ-μ_1 and different liquid cooling plate

Fig. 19. Curve graph of the θ-μ_1 relationship

As shown in Fig. 19 (a) the comprehensive performance under the 2 g/s operating condition is the most remarkable. This condition can not only maintain the maximum temperature within a reasonable range below 318.15K but also ensure a relatively uniform temperature distribution. Although the pressure drop has increased, it has not yet reached an unacceptable level. In contrast, the temperature control capacity of the 0.5 g/s operating condition is inadequate, while the 2.5 g/s operating condition exhibits excessive energy consumption.

As shown in Fig. 19 (b) compared with other inlet temperature conditions, at 298.15 K, the battery pack can establish a more reasonable matching relationship between the maximum temperature control and temperature uniformity, without causing additional deterioration in flow performance.

As shown in Fig. 19 (c) through a comparison of several distinct environmental temperature conditions, it is observable that at 298.15 K, the battery pack can establish a relatively well-coordinated matching relationship among the highest temperature control, temperature uniformity, and the flow performance of the liquid cooling system.

Under the baseline conditions of a 5C discharge rate, an inlet flow rate of 2 g/s, an ambient temperature of 298.15 K, an inlet temperature of 298.15 K, and a discharge duration of 720 s, the battery pack temperature, temperature difference, pressure drop, and other data of the three liquid-cooled structures—parallel, intermittent, and slanted channels—were obtained and recorded, as shown in Fig. 19 (d) the θ value curve of the parallel liquid cooling channel shows an overall increasing trend, while the θ value curves of the intermittent and oblique liquid cooling channels both show a decreasing trend, with the oblique liquid cooling channel curve consistently at the bottom of the graph, indicating the best overall cooling performance. The overall variation range of the oblique liquid cooling channel is the smallest, indicating the lowest sensitivity to weight changes, maintaining optimal overall performance across the entire weight space, fully demonstrating the superiority of the oblique liquid cooling channel design.

4.CONCLUSION

In this paper, a composite cooling battery pack thermal management system incorporating phase change materials, biomimetic fins, and liquid cooling plates was constructed. Firstly, the performance differences among the three schemes - pure phase change cooling, fin-enhanced phase change cooling,

and composite cooling - under a 5C discharge rate were compared. The results showed that the maximum temperature of the battery pack was reduced to below 318 K by the composite cooling system, which was more than 8 K lower than the pure phase change scheme. Moreover, the liquid phase distribution of the phase change material was more uniform, and the system had good thermal buffering and continuous cooling capabilities. Secondly, three flow channel structures - parallel, intermittent, and Oblique cut channel was designed for the liquid cooling plate, and comparative analyses were conducted in terms of battery temperature distribution, uniformity, and pressure drop. The Oblique cut channel liquid cooling channel had the best comprehensive performance under different weight preferences, and could achieve the best temperature control effect and temperature uniformity with a moderate pressure drop increase. Further studies were conducted on the influence of cooling fluid flow rate (0.5-2.5 g/s), inlet temperature (288.15-308.15 K), and ambient temperature (293.15-313.15 K) on the system performance. The results showed that an increase in flow rate could lower the maximum battery temperature, but the marginal benefit decreased. 2 g/s was the reasonable flow rate that balanced cooling effect and energy consumption economy. When the inlet temperature was 298.15 K, the system had the best comprehensive performance. When the ambient temperature was higher than this value, the cooling effect and temperature uniformity would be significantly deteriorated. This research provided design basis and parameter references for the engineering application of the composite cooling system.

FUNDING

This work is supported by State Key Laboratory of Safe Mining of Deep Coal and Environmental Protection, Huainan Mining (Group) Co., Ltd. (Grant No. 2025YB008)

CONFLICT OF INTEREST

The authors declare that they have no known competing financial interests or personal relationships that could have appeared to influence the work reported in this paper.

REFERENCES

[1] Y.-S. Duh, Y. Sun, X. Lin, J. Zheng, M. Wang, Y. Wang, X. Lin, X. Jiang, Z. Zheng, S. Zheng, G. Yu, Characterization on thermal runaway of commercial 18650 lithium-ion batteries used in electric vehicles: A review, Journal of Energy Storage 41 (2021). http://dx.doi.org/10.1016/j.est.2021.102888

[2] D. Balasubramanian, I.P. Venugopal, M. Subramanian, V. Raja, U. Kale, J. Matijošius, Study on the battery thermal management system for cylindrical lithium-ion battery with nano-doped phase change material and liquid cooling, Scientific Reports 15(1) (2025). http://dx.doi.org/10.1038/s41598-025-08884-5

[3] V. Etacheri, R. Marom, R. Elazari, G. Salitra, D. Aurbach, Challenges in the development of advanced Li-ion batteries: a review, Energy & Environmental Science 4(9) (2011). http://dx.doi.org/10.1039/c1ee01598b

[4] J.B. Goodenough, K.-S. Park, The Li-Ion Rechargeable Battery: A Perspective, Journal of the American Chemical Society 135(4) (2013) 1167-1176. http://dx.doi.org/10.1021/ja3091438

[5] B. Dunn, H. Kamath, J.M. Tarascon, Electrical Energy Storage for the Grid: A Battery of Choices, Science 334(6058) (2011) 928-935. http://dx.doi.org/10.1126/science.1212741

[6] R. Zhou, Y. Chen, J. Zhang, P. Guo, Research progress in liquid cooling technologies to enhance the

thermal management of LIBs, Materials Advances 4(18) (2023) 4011-4040. http://dx.doi.org/10.1039/d3ma00299c

[7] A.A. Pesaran, Thermal Performance of EV and HEV Battery Modules and Packs, National Renewable Energy Laboratory (1997). http://dx.doi.org/https://doi.org/10.1016/S0378-7753(02)00200-8

[8] S. Ma, M. Jiang, P. Tao, C. Song, J. Wu, J. Wang, T. Deng, W. Shang, Temperature effect and thermal impact in lithium-ion batteries: A review, Progress in Natural Science: Materials International 28(6) (2018) 653-666. http://dx.doi.org/10.1016/j.pnsc.2018.11.002

[9] J. Jaguemont, L. Boulon, Y. Dubé, A comprehensive review of lithium-ion batteries used in hybrid and electric vehicles at cold temperatures, Applied Energy 164 (2016) 99-114. http://dx.doi.org/10.1016/j.apenergy.2015.11.034

[10] J.P.C. Chester G. Motloch, Jeffrey R. Belt, Randy B. Wright, Gary L. Hunt, PNGV Battery Testing Procedures And Analytical Methodologies For HEV's, (2002). http://dx.doi.org/10.4271/2002-01-1950

[11] Qingsong Wanga, Ping Pinga, Xuejuan Zhaoa, Guanquan Chub, Jinhua Suna,∗, Chunhua Chenc, Thermal runaway caused fire and explosion of lithium ion battery, Journal of Power Sources 208 (2012) 210-224. http://dx.doi.org/https://doi.org/10.1016/j.jpowsour.2012.02.038

[12] J. E, H. Xiao, S. Tian, Y. Huang, A comprehensive review on thermal runaway model of a lithium-ion battery: Mechanism, thermal, mechanical, propagation, gas venting and combustion, Renewable Energy 229 (2024). http://dx.doi.org/10.1016/j.renene.2024.120762

[13] L.H. Saw, Y.H. Ye, A.A.O. Tay, Electrochemical-thermal analysis of 18650 Lithium Iron Phosphate cell, Energy Conversion and Management 75 (2013) 162-174. http://dx.doi.org/10.1016/j.enconman.2013.05.040

[14] S. Panchal, I. Dincer, M. Agelin-Chaab, R. Fraser, M. Fowler, Thermal modeling and validation of temperature distributions in a prismatic lithium-ion battery at different discharge rates and varying boundary conditions, Applied Thermal Engineering 96 (2016) 190-199. http://dx.doi.org/10.1016/j.applthermaleng.2015.11.019

[15] J. Kim, J. Oh, H. Lee, Review on battery thermal management system for electric vehicles, Applied Thermal Engineering 149 (2019) 192-212. http://dx.doi.org/10.1016/j.applthermaleng.2018.12.020

[16] G.D. Xia, L. Cao, G.L. Bi, A review on battery thermal management in electric vehicle application, Journal of Power Sources 367 (2017) 90-105. http://dx.doi.org/10.1016/j.jpowsour.2017.09.046

[17] Z.H. Rao, S.F. Wang, A review of power battery thermal energy management, Renew. Sust. Energ. Rev. 15(9) (2011) 4554-4571. http://dx.doi.org/10.1016/j.rser.2011.07.096

[18] Y.B. Suhua. C, Research Progress on Thermal Runaway Mechanism and Thermal Management Technology of Lithium-ion Power Batteries, China Science Foundation 37(2) (2023) 187-198.

[19] J.Q. Wang, Y.H. Gan, J.L. Liang, M.X. Tan, Y. Li, Sensitivity analysis of factors influencing a heat pipe-based thermal management system for a battery module with cylindrical cells, Applied Thermal Engineering 151 (2019) 475-485. http://dx.doi.org/10.1016/j.applthermaleng.2019.02.036

[20] Y.H. Huang, W.L. Cheng, R. Zhao, Thermal management of Li-ion battery pack with the application of flexible form-stable composite phase change materials, Energy Conversion and Management 182

(2019) 9-20. http://dx.doi.org/10.1016/j.enconman.2018.12.064
[21] M. Murugan, P.V. Elumalai, K.C.K. Vijayakumar, M. Babu, K.S. Kumar, M. Ganesh, L. Kuang, S. Prabhakar, A Comprehensive Review of Thermal Management Methods and Ideal System Design for Improved Electric Vehicle Battery Pack Performance and Safety, Energy Science & Engineering 13(3) (2025) 1011-1036. http://dx.doi.org/10.1002/ese3.2081
[22] Y.Z. Zhao, X.L. Zhang, B. Yang, S.W. Cai, A review of battery thermal management systems using liquid cooling and PCM, Journal of Energy Storage 76 (2024) 20. http://dx.doi.org/10.1016/j.est.2023.109836
[23] H.Z. Yang, M.X. Li, Z.H. Wang, B.J. Ma, A compact and lightweight hybrid liquid cooling system coupling with Z-type cold plates and PCM composite for battery thermal management, Energy 263 (2023) 14. http://dx.doi.org/10.1016/j.energy.2022.126026
[24] S. Mousavi, A. Zadehkabir, M. Siavashi, X.H. Yang, An improved hybrid thermal management system for prismatic Li-ion batteries integrated with mini-channel and phase change materials, Applied Energy 334 (2023) 16. http://dx.doi.org/10.1016/j.apenergy.2023.120643
[25] L.L. XinXin Jiang, Optimization of Thermal Management Performance for Lithium-Ion Batteries Combining Phase Change Materials and Liquid Cooling, Journal of Shanghai University of Science and Technology 46(1) (2024) 36-43. http://dx.doi.org/10.13255/j.cnki.jusst.20220405001
[26] H. Choi, H.Y.S. Lee, U.K. Han, J.E.Y. Jung, H.S. Lee, Comparative Evaluation of Liquid Cooling-Based Battery Thermal Management Systems: Fin Cooling, PCM Cooling, and Intercell Cooling, International Journal of Energy Research 2024 (2024) 23. http://dx.doi.org/10.1155/2024/5395508
[27] J.H. Pu, Y. Li, R.C. Li, N. Hua, H. Zhang, Y.C. Lu, S. Panchal, R. Fraser, M. Fowler, X.K. Zhang, Design and performance of a compact lightweight hybrid thermal management system using phase change material and liquid cooling with a honeycomb-like structure for prismatic lithium-ion batteries, Journal of Power Sources 624 (2024) 12. http://dx.doi.org/10.1016/j.jpowsour.2024.235632
[28] R. El Kassar, A. Al Takash, J. Faraj, M. Hammoud, M. Khaled, H.S. Ramadan, Recent advances in lithium-ion battery integration with thermal management systems for electric vehicles: A summary review, Journal of Energy Storage 91 (2024) 12. http://dx.doi.org/10.1016/j.est.2024.112061
[29] M.X. Luo, Y.X. Zhang, Z.H. Wang, Y.Y. Niu, B.H. Lu, J.J. Zhu, J.Y. Zhang, K. Wang, Thermal performance enhancement with snowflake fins and liquid cooling in PCM-based battery thermal management system at high ambient temperature and high discharge rate, Journal of Energy Storage 90 (2024) 12. http://dx.doi.org/10.1016/j.est.2024.111754
[30] A.J.H. Hareth Maher Abd, Abdual Hadi N. Khalifa, Hybrid battery thermal management system of phase change materials integrated with aluminum fins and forced air, Energy Storage 6 (2024). http://dx.doi.org/10.1002/est2.625
[31] P.M. Sutheesh, A.P. Atul, B. Rohinikumar, Numerical and experimental investigations of thermal performance of lithium-ion battery with hybrid cooling system under dry-out condition, Journal of Energy Storage 84 (2024) 20. http://dx.doi.org/10.1016/j.est.2024.110889
[32] P.E. Bernardi D, Newman J, A General Energy Balance for Battery Systems, Journal of the Electrochemical Society 132 (1985) 5-12. http://dx.doi.org/10.1149/1.2113792

[33] X. Fan, C. Meng, Y. Yang, J. Lin, W. Li, Y. Zhao, S. Xie, C. Jiang, Numerical optimization of the cooling effect of a bionic fishbone channel liquid cooling plate for a large prismatic lithium-ion battery pack with high discharge rate, Journal of Energy Storage 72 (2023). http://dx.doi.org/10.1016/j.est.2023.108239